

# Magnetic probe for material characterization at optical frequencies

Tomasz J. Antosiewicz<sup>a,b\*</sup>, Piotr Wróbel,<sup>c</sup> and Tomasz Szoplik<sup>c</sup>

<sup>a</sup>Interdisciplinary Centre for Mathematical and Computational Modelling, University of Warsaw, Pawinskiego 5A, 02-106 Warsaw, Poland;

<sup>b</sup>Department of Applied Physics, Chalmers University of Technology, SE-412 96 Göteborg, Sweden;

<sup>c</sup>Faculty of Physics, University of Warsaw, Pasteura 7, 02-093 Warszawa, Poland

## ABSTRACT

Rapid development of novel, functional metamaterials made of purely dielectric, plasmonic, or composite structures which exhibit tunable optical frequency magnetic responses creates a need for new measurement techniques. We propose a method of actively measuring magnetic responses, *i.e.* magnetic dispersion, of such metamaterials within a wide range of optical frequencies with a single probe by exciting individual elementary cells within a larger matrix. The probe is made of a tapered optical fiber with a radially corrugated metal coating. It concentrates azimuthally polarized light in the near-field below the apex into a subwavelength size focus of the longitudinal magnetic field component. An incident azimuthally polarized beam propagates in the core until it reaches the metal stripes of constant angular width running parallel to the axis. For a broad frequency range light-to-plasmon coupling is assured as the lattice constant changes with the radius due to constant angular width. Bound plasmonic modes in slits between the metal stripes propagate toward the apex where circular currents in stripes and displacement currents in slits generate a strong longitudinal magnetic field. The energy density of the longitudinal magnetic component in the vicinity of the axis is much stronger than that of all the other components combined, what allows for pure magnetic excitation of magnetic resonances rather than by the electric field. The scattered signal is then measured in the far-field and analyzed.

**Keywords:** Surface plasmons, scanning microscopy, integrated optics devices, metamaterials, magneto-optical materials.

## 1. INTRODUCTION

Measurements of dispersionless magnetic susceptibility  $\chi_m$  of materials are performed with Evans type balances which measure the force applied to a sample located in a magnetic field.<sup>1</sup> Due to recent activities in the fields of material science, nanotechnology, and photonics, new composite substances have been designed and fabricated, *e.g.* metamaterials, which are characterised by engineered *dispersion* of both permittivity and permeability. Magnetic resonances have been moved into THz and optical frequencies with their intensity in artificial materials being stronger than in natural ones.<sup>2-8</sup> Metamaterial building blocks of linear sizes  $L \ll \lambda$  can take the form of Swiss rolls with negative permeability in microwave frequencies,<sup>2,3</sup> split ring resonators and wires,<sup>4-6</sup> and fishnet with a negative real part of the refractive index in the range from microwave to optical.<sup>7,8</sup> The magnetic response of these structures becomes weaker at frequencies higher than 100 THz because of internal resistance which scales inversely with frequency.<sup>9,10</sup> It is in accordance with a XX century idea that effects connected with magnetic susceptibility are negligible in high frequencies. Nevertheless, metamaterials with resonances at THz frequencies can be made of a variety of base elements, *e.g.* dielectric particles of high permittivity,<sup>11-15</sup> noble metals,<sup>16,17</sup> and aluminum.<sup>18</sup>

Measurements of magnetic properties of bulk materials are, at least in principle, straightforward, however, they become more complicated if properties of individual building blocks/elementary cells are in question. With the shift of tunable magnetic responses of metamaterials into IR and optical frequencies new characterization

---

\*tantos@igf.fuw.edu.pl, tomasza@chalmers.se

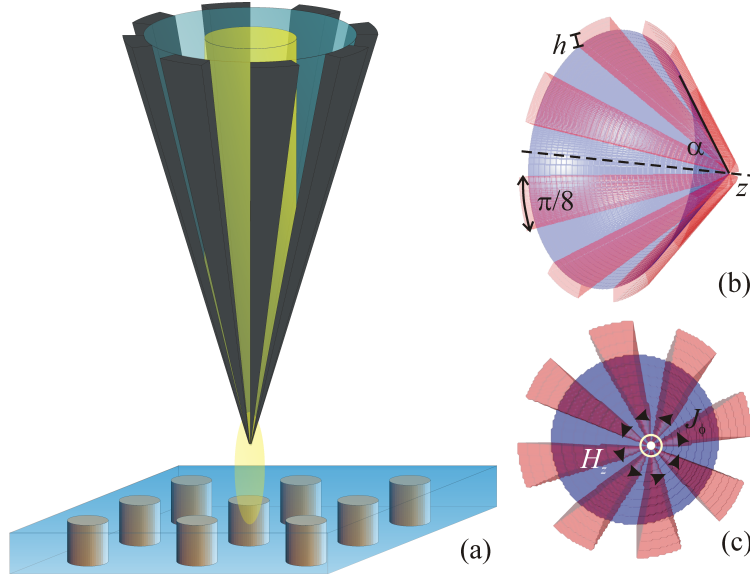


Figure 1. (a) Probe for magnetic measurements: a dielectric probe with a metal grating concentrates the longitudinal magnetic component of light into a subwavelength spot to measure the magnetic moment of individual metamaterial elementary cells. (b) The tapered at angle  $\alpha$  part of a fiber probe with eight equidistant slits and eight  $h$  thick silver lands of constant angular width equal  $\pi/8$ . (c) Azimuthal currents  $J_\phi$ , indicated by black arrowheads, generate the longitudinal magnetic field  $H_z$  shown by a white out-of-plane vector.

techniques are needed. Burrese *et al.* have reported on near-field detection of the magnetic field of light using an aperture scanning near-field optical microscope (SNOM) probe with a split ring resonator (SRR) in the aperture plane.<sup>19</sup> Also, aperture probes without an SRR allowed passive measurements of the magnetic component of modes excited in photonic crystal cavities coupled to waveguides.<sup>20,21</sup> Another experimental method of independently testing the electric and magnetic resonances of a properly oriented SRR by means of a y-polarized  $\text{TEM}_{10}$  mode (y-polarized  $\text{HG}_{01}$  mode<sup>22</sup>) with a strongly focused on-axis longitudinal magnetic field  $H_z$  and off-axis  $E_y$  components was proposed by Banzer *et al.*<sup>23</sup>

## 2. CONCENTRATING THE MAGNETIC FIELD

In this report we describe a probe able to concentrate the magnetic component of an electromagnetic wave into a longitudinal spot with a subdiffraction diameter.<sup>24</sup> It is functional within a broad, including the optical, spectrum for measurements of magnetic resonances of elementary cells of metamaterials composed of all-dielectric and plasmonic structures. The elementary cell sizes can be of linear dimensions down to hundreds of nanometers and their limit is determined by geometrical size of the probe aperture plane. The magnetic field concentrator, shown in Fig. 1a, is composed of a dielectric cone, *e.g.* a tapered fiber probe, with a metal grating of lattice constant decreasing toward the tip end. It excites magnetic resonances in the near-field in a manner similar to conventional SNOM.

An azimuthally polarized, cylindrically symmetric light beam (Laguerre-Gauss  $\text{TE}_{10}$  mode<sup>22</sup>) couples to plasmons supported by the silver grating, see Fig. 1b. Plasmons propagate along the silver stripes toward the end-plane of the probe, where they generate a confined longitudinal magnetic field component  $H_z$  with energy densities exceeding those of other components by more than an order of magnitude, as indicated schematically in Fig. 1c. The sample, which is below the probe, is penetrated by the field which induces directly (using the magnetic field  $H_z$ ) a magnetic resonance in a metamaterial elementary cell. The scattered signal is measured in the far-field using a classical intensity detector, giving information on the properties of the sample. This magnetic concentrator is analogous to SNOM metal-coated tapered fiber probes with a corrugated core surface,<sup>25–27</sup> where grooves enhance coupling of incident light to surface plasmons.

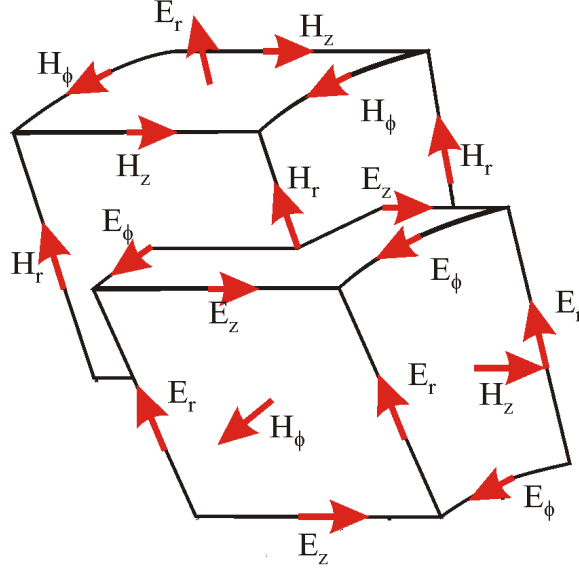


Figure 2. Schematic representation of the Yee grid and electromagnetic field vector nodes in cylindrical coordinates.

## 2.1 Magnetic probe structure

The core of the magnetic concentrator (Fig. 1) is a cone composed of a dispersionless dielectric of permittivity  $\epsilon = 2.1$  and the cone has a half-angle equal to  $40^\circ$ . It is a usual dielectric tapered fiber used for SNOM probes, however, in the current investigations we omit the fiber cladding and set the core diameter to  $3.2 \mu\text{m}$ . The metal lands and the slits have constant angular width equal  $\pi/8$  (eight periods total), what means that their lattice periodicity decreases toward the apex assuring momentum matching for excitation of plasmons by light for a wide range of wavelengths. The metal lands are made of silver (thickness  $h$  varied from 0 to 100 nm), which is a very good material for guiding plasmons due to its low losses. It is modeled using Drude dispersion  $\epsilon(\omega) = \epsilon_\infty - \omega_p^2/[\omega(\omega + i\Gamma)]$  fitted to experimental data obtained by Johnson and Christy<sup>28</sup> with parameters equal  $\epsilon_\infty = 3.70$ ,  $\omega_p = 13673 \text{ THz}$ , and  $\Gamma = 27.35 \text{ THz}$

## 3. FINITE-DIFFERENCE TIME-DOMAIN SIMULATIONS IN CYLINDRICAL COORDINATES

Results presented in this paper are calculated using the finite-difference time-domain (FDTD) method.<sup>29</sup> Contrary to our previous works with corrugated SNOM probes<sup>25-27</sup> which are cylindrically symmetric, the magnetic probe lacks that property. Its dimensions vary from relatively large (ca. 500 nm) far from the apex to very small at the apex (ca. 5 nm), so a variable geometry grid is necessary for an accurate and feasible simulation. At the same time a cartesian grid is not optimal due a mismatch between it and a cylindrical profile of the structure. Such mismatches result in generation of purely numerical solutions which should be avoided. The easiest and most natural solution is to mesh the probe and simulation volume using a cylindrical Yee grid as shown in Fig. 2. Even though this procedure complicates the simulation slightly, as separate equations for the axis fields update are needed, it is optimal because of fine sampling near to the axis due to constant angular discretization. The field update equations are derived from Maxwell's Equations

$$\frac{\partial E_r}{\partial t} = \frac{1}{\epsilon\epsilon_0} \left[ \frac{1}{r} \frac{\partial H_z}{\partial \phi} - \frac{\partial H_\phi}{\partial z} \right] - \frac{\sigma}{\epsilon\epsilon_0} E_r, \quad \frac{\partial H_r}{\partial t} = -\frac{1}{\mu\mu_0} \left[ \frac{1}{r} \frac{\partial E_z}{\partial \phi} - \frac{\partial E_\phi}{\partial z} \right] - \frac{\sigma^*}{\mu\mu_0} H_r, \quad (1)$$

$$\frac{\partial E_\phi}{\partial t} = \frac{1}{\epsilon\epsilon_0} \left[ \frac{\partial H_r}{\partial z} - \frac{\partial H_z}{\partial r} \right] - \frac{\sigma}{\epsilon\epsilon_0} E_\phi, \quad \frac{\partial H_\phi}{\partial t} = -\frac{1}{\mu\mu_0} \left[ \frac{\partial E_r}{\partial z} - \frac{\partial E_z}{\partial r} \right] - \frac{\sigma^*}{\mu\mu_0} H_\phi, \quad (2)$$

$$\frac{\partial E_z}{\partial z} = \frac{1}{\epsilon\epsilon_0} \frac{1}{r} \left[ \frac{\partial}{\partial r} (rH_\phi) - \frac{\partial H_r}{\partial \phi} \right] - \frac{\sigma}{\epsilon\epsilon_0} E_z, \quad \frac{\partial H_z}{\partial z} = -\frac{1}{\mu\mu_0} \frac{1}{r} \left[ \frac{\partial}{\partial r} (rE_\phi) - \frac{\partial E_r}{\partial \phi} \right] - \frac{\sigma^*}{\mu\mu_0} H_z, \quad (3)$$

where  $\epsilon$ ,  $\mu$  are relative permittivity and permeability, respectively, with 0 denoting those of vacuum, and  $\sigma$  and  $\sigma^*$  are electric and magnetic conductivity, respectively. The derivatives are now converted into finite differences in time and space yielding the main FDTD update equations. For example, the  $E_r$  is

$$E_r|_{i+\frac{1}{2},j+\frac{1}{2},k}^{n+\frac{1}{2}} = \frac{2\epsilon\epsilon_0 - \sigma\Delta t}{2\epsilon\epsilon_0 + \sigma\Delta t} E_r|_{i+\frac{1}{2},j+\frac{1}{2},k}^{n-\frac{1}{2}} + \frac{2\Delta t}{2\epsilon\epsilon_0 + \sigma\Delta t} \left( \frac{H_z|_{i+\frac{1}{2},j+1,k}^n - H_z|_{i+\frac{1}{2},j,k}^n}{\Delta\phi \cdot \Delta r (i + \frac{1}{2})} - \frac{H_\phi|_{i+\frac{1}{2},j+\frac{1}{2},k+\frac{1}{2}}^n - H_\phi|_{i+\frac{1}{2},j+\frac{1}{2},k-\frac{1}{2}}^n}{\Delta z} \right), \quad (4)$$

where indices  $i$ ,  $j$ , and  $k$  enumerate grid nodes in  $r$ ,  $\phi$ , and  $z$  directions,  $n$  indexes time steps,  $\Delta r$ ,  $\Delta\phi$ , and  $\Delta z$  are grid resolution, and  $\Delta t$  is the time step. Expressions for other components can be easily obtained.

A critical point in these simulations is numerical stability influenced by the temporal discretization. In a cubical cartesian grid the largest time step is  $\Delta x/c\sqrt{3}$ , where  $\Delta x$  is the uniform spatial step and  $c$  is the speed of light. For greater stability it may be decreased and we usually use  $\Delta t_\square = \Delta r/2c$ , however, this does not apply in our simulations, as the azimuthal discretization forces a very fine mesh near the axis equal  $\Delta\phi \cdot \Delta r/2$ . The actual time step in cylindrical coordinates is  $\Delta t = \Delta\phi \cdot \Delta r / (c\sqrt{4 + 2\Delta\phi^2}) \approx \Delta\phi \cdot \Delta t_\square$ . This approximation is quite good for 100 azimuthal grid lines. As it can be seen, this method is quite costly in terms of simulation time. While the simulated probe is not rotationally symmetric, due to eight slit-land periods it has an 8-fold symmetry. We utilise this fact to shrink the simulation volume to one-eighth of the original by imposing periodic boundary conditions. The incident wave is an azimuthally polarized TE<sub>01</sub> Laguerre-Gauss beam which does not forbid us from employing this trick.

In simulations we analyze steady state and transient responses of the magnetic probe to assess its ability to concentrate the magnetic field, *i.e.* the magnetic-to-electric energy densities ratio in the focus, the full-width at half-maximum (FWHM) of the magnetic focus, and concentration efficiency. The transient calculations are performed for a temporal Gaussian pulse centered at 600 nm modulated by a sine function and the spectra are calculated by Fourier-transformation. The steady state analysis with a cw-beam is carried out mainly to visualise the field distribution in the entire volume for different structures.

#### 4. BEAMING THE MAGNETIC FIELD

In Fig. 3 we present how the electromagnetic energy density in a magnetic probe is distributed among the field components. An azimuthally polarized beam of wavelength  $\lambda = 500$  nm (chosen as an example) enters the radially corrugated magnetic probe from the right side and is transformed by the device into a localized magnetic needle at the axis on the left side of the apex. The incident field couples the silver stripes to generate plasmons which propagate toward the apex. The plasmons between the slits have a dominant, azimuthal component which is preserved during propagation. This azimuthal field, which stops propagating as plasmons upon reaching the apex, is responsible for generating a longitudinal magnetic field  $H_z$  beyond the apex plane with a spot size of about 185 nm. Beside the longitudinal field, other components (aligned according to decreasing energy density) exist:  $E_\phi$ ,  $H_r$ , and  $E_z$ . The energy densities of  $E_\phi$  and  $H_r$  are zero at the axis and reach their respective maximums 800 nm from the axis (the  $H_z$  FWHM is 185 nm), while the  $E_z$  energy density is more than one order of magnitude weaker than that of  $H_z$ . In the case of  $E_\phi$  and  $H_r$ , the strongest side lobes at  $r = 800$  nm originate from part of the incident beam passing directly through the gaps between the metal stripes, because at that radius the slit width is larger than 300 nm. A probe with a bigger core radius and a wider beam will have

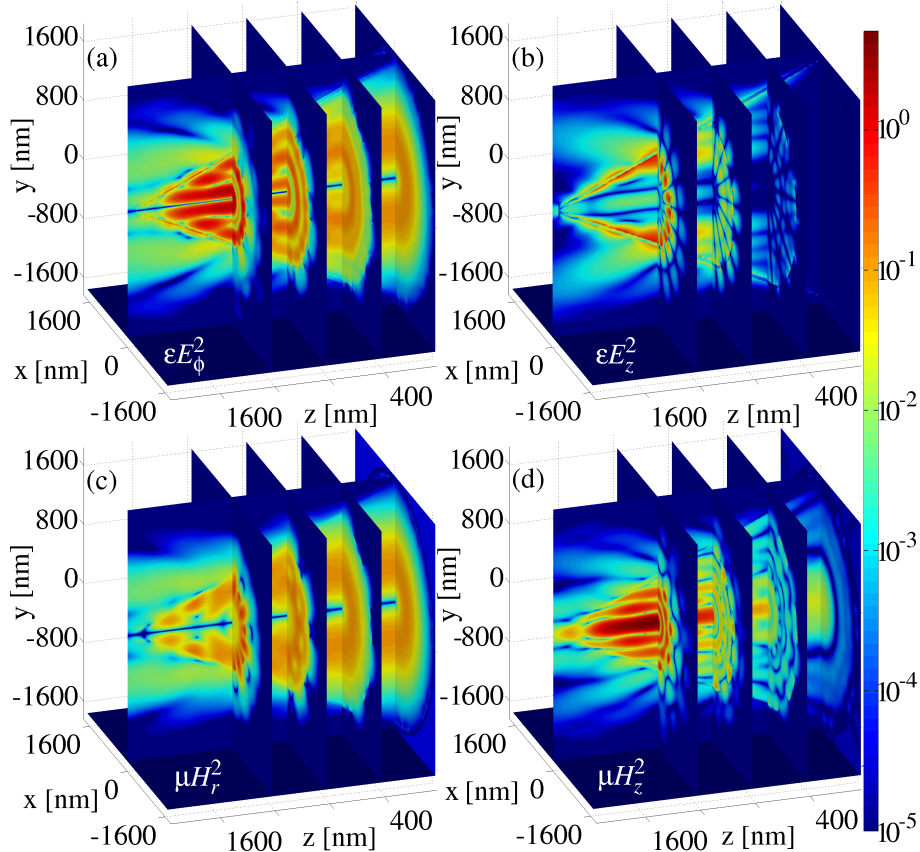


Figure 3. Electromagnetic field in the tapered part of the probe with 50 nm silver layer: energy density of (a) azimuthal electric field  $\epsilon E_\phi^2$ , (b) longitudinal field  $\epsilon E_z^2$ , (c) radial magnetic field  $\mu H_r^2$ , (d) longitudinal  $\mu H_z^2$ . The pseudocolor scale is logarithmic and in arbitrary units, wavelength  $\lambda = 500$  nm is used as an example. The probe apex is located at the plane  $z_a \approx 1900$  nm.

side lobes farther away, so optical fibers with larger cores than considered here will have an even smaller overlap of the components than obtained here. In addition to the maximum at 800 nm,  $E_\phi$  and  $H_r$  have less intensive side lobes closer to the axis at about 400 nm.

#### 4.1 Spot size

Light concentration into subwavelength spots by tapered metal structures is one of the cornerstones of plasmonics.<sup>30–33</sup> The first parameter determining the probe's usefulness we investigate is the spot size defined at the FWHM. It decides upon the dimensions of the elementary cells of artificial materials that can be probed. The magnetic probe in its current form generates a strong magnetic field as seen in Fig. 3, but also allows for light to leak out through its sides. While this leakage should be eliminated through the use of Al coating, we investigate how the spot size depends on the probe parameters and whether the leakage affects the spot size.

Figure 4 shows the FWHM of the focused magnetic field  $H_z$  in the analysed wavelength range for all considered silver stripe thicknesses  $h$ . The spot size of magnetic probes is almost always smaller than for an all-dielectric probe ( $h = 0$  nm). The FWHM decreases slowly with decreasing wavelength and is the lowest for the largest thickness. This is because formation of the  $H_z$  needle is governed by azimuthal currents  $J_\phi$  and displacement currents flowing through stripes and slits, respectively, and by the azimuthal component  $E_\phi$  of part of the electric field refracted leaving the probe. The contribution from the refracted  $E_\phi$  diminishes as  $h$  increases, so the FWHM is determined by  $J_\phi$  and edge modes.

The plasmon modes supported by the grating depend strongly on the distance from the axis, because volume between the slits increases linearly with radius  $r$ . For a large  $r$  plasmons form a coupled mode at both inner and

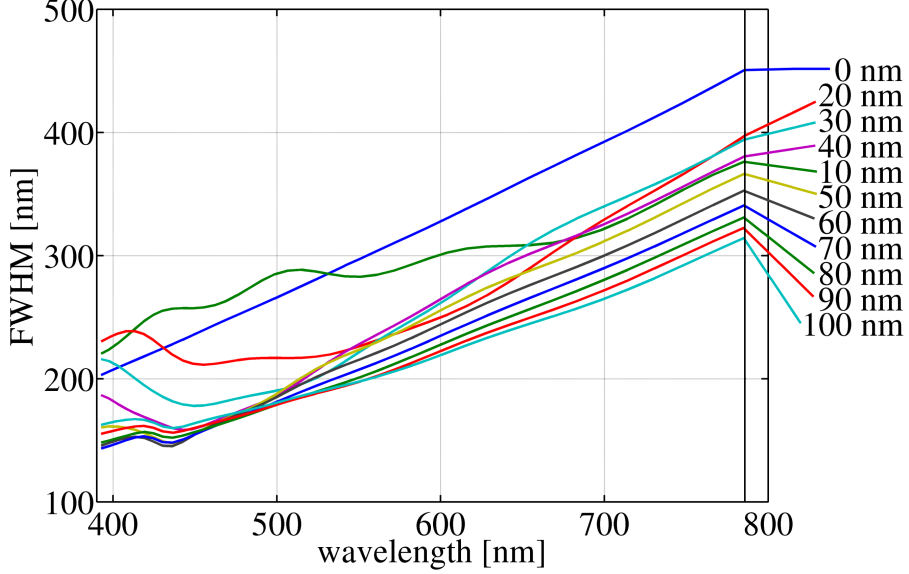


Figure 4. Full-width at half-maximum of the longitudinal magnetic field component  $H_z$  calculated 10 nm from the apex for Ag stripe thicknesses  $h \in [0, 100]$  nm.

outer edges. As they propagate forward  $r$  becomes smaller and the groove width decreases, what results in mode decoupling and the inside one experiences a cut-off before reaching the apex, and only the outer one remains. If the silver thickness  $h$  is large enough, then the mode remains confined at the outer edges, as discussed in a similar case<sup>34</sup> on V-grooves, until it reaches the probe apex where it radiates forming a  $H_z$  needle. However, for small  $h$  plasmons will radiate into an azimuthally polarized beam before reaching the apex and diffraction enlarges the spot size considerably. For example, the wide FWHM values observed for  $h = 10 \div 30$  nm are explained by very weak guiding provided by the silver lands. Moreover, instead of coupling to plasmons guided by silver stripes, light leaks out of the dielectric core forming a strong background signal comparable to that of an all-dielectric probe. The decoupling naturally depends on the wavelength and occurs the farther from the apex for larger  $\lambda$ . Thus, the silver thickness  $h$ -to-wavelength  $\lambda$  ratio determines the spot size, however, we observe saturation of this rule at around 480 nm.

At this wavelength for  $h \geq 40$  nm the FWHMs become equal due to an equilibrium between the enlargement of the spot size by early decoupling for small  $h$  and direct enlargement due to a large  $h$ . For  $h \geq 60$  nm and  $\lambda < 450$  nm the FWHM order is reversed due to the decoupling cut-off being smaller than the thickness for short wavelengths. However, as  $h$  decreases ( $h \leq 50$  nm) below the cut-off, plasmons decouple before the apex and their FWHM at the sample position increases.

## 4.2 Energy efficiency

The FWHM plot and field distributions show that the probe generates a longitudinal magnetic field beyond the apex, however, we still need to confirm that its energy density is greater than that of other components. This is illustrated by Fig. 5 which presents energy densities of four field components (Fig. 5(a)  $E_\phi$ , (b)  $E_z$ , (c)  $H_r$ , (d)  $H_z$ ) integrated over an area of diameter equal to the FWHM of  $H_z$ . The energy density of field components increases with an increasing  $h$ , because thick stripes are more efficient at confining and guiding energy toward the apex than thin ones. For small  $h$ , refraction of the beam by the dielectric core becomes strong compared to the influence of the silver stripes, what explains weak polarization cross-coupling by a structure composed mostly of an all-linear-dielectric. The longitudinal electric field  $E_z$  for  $h = 20$  nm is negligible, while the energy densities of  $E_\phi$ ,  $H_r$ , and  $H_z$  are not similar to those of larger  $h$  values. This supports the observation that stripes 20 nm thick are an intermediate between a mostly dielectric-dependent and a predominantly plasmonic response of the magnetic probe.

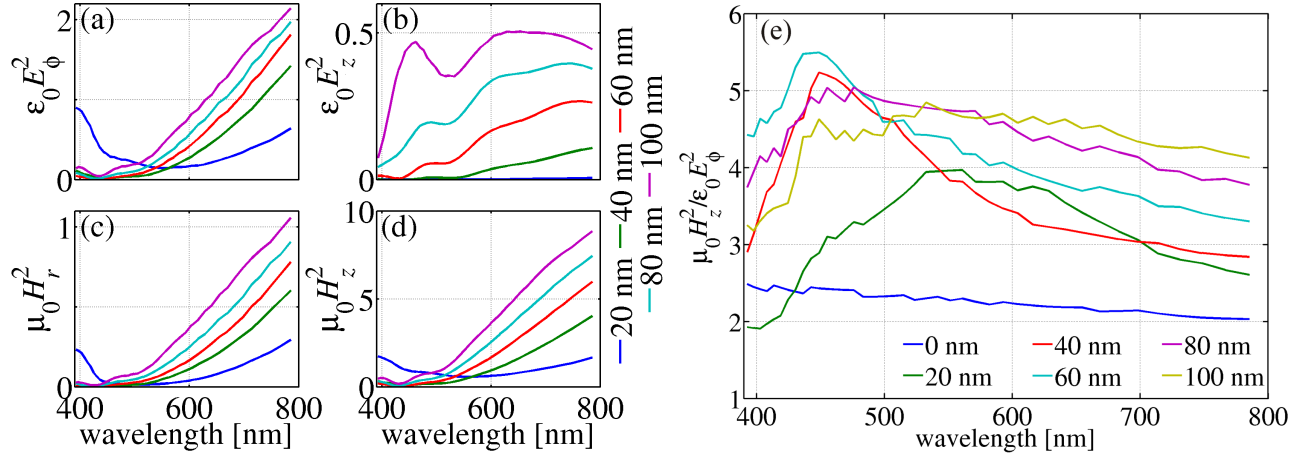


Figure 5. Total energy densities of electromagnetic field components (a)  $E_\phi$  (b)  $E_z$  (c)  $H_r$  (d)  $H_z$  integrated 10 nm from the apex in the focus where  $H_z$  is dominant. Units are arbitrary and the same for all subfigures. (e) Ratio of total  $H_z$  energy density to  $E_\phi$  energy density.

Most efficient pure magnetic excitation of magnetic resonances depends not only on the presence of a particular  $H$ -field component, but also on a lack of electric-field coupling to the measured structure. Let us look at the ratio of the  $H_z$  energy density to the electric energy density of  $E_\phi$  shown in Fig. 5e. The dielectric probe considered as a reference structure displays, as expected, a linear dependence of  $\mu H_z^2/(\epsilon E_\phi^2) < 2.5$  in the optical range. When we add the silver grating the ratio increases up to 5.5 for  $h = 60$  nm at  $\lambda = 450$  nm, however, this peak is narrow. For  $h$  equal to 80 and 100 nm the ratio is lower in the respective peaks than for  $h = 60$  nm, but the peaks are quite wide and for a large wavelength range stay above 4. The reason for the appearance of the peaks in Fig. 5b,e and their dependence on  $h$  are the same as for the FWHM minimum in Fig. 4. It is a trade-off between the outer mode cut-off and a large  $h$  guiding energy away from the axis. This is modulated by diffraction, which is stronger for larger wavelengths if the system dimensions are the same. Thus, radially corrugated probes with thick metalisation are more efficient at focusing the magnetic field in terms of localizing magnetic energy density as well as generating small FWHMs than those with small  $h$ .

## 5. CONCLUSIONS

We have described theoretically a novel device for generating a strong longitudinal magnetic field for direct, active measurements of magnetic resonances in the optical range. The proposed device is based on a tapered dielectric core akin to SNOM probes and in principle may be used in near-field microscopes with a classical shear force control of the probe-sample distance. The near-field magnetic needle is used to generate magnetic responses of elementary cells and the scattered light is recorded with intensity detectors in the far-field. Using this technique it will be possible to test individual metamaterial building blocks with sizes down to 160 nm for short wavelengths. Once materials with optically induced magnetism are developed the proposed magnetic field concentrator may be used for magnetic write/read operations.

## ACKNOWLEDGMENTS

This work was supported by the Polish Ministry of Science and Higher Education under the projects N N202 302638 and Iuventus Plus 0480/H03/2010/70 and the National Centre for R&D under the project N R15 0018 06. The authors are partners in COST Actions MP 0702 and MP 0803. Simulations were performed at the Interdisciplinary Centre for Mathematical and Computational Modelling at the University of Warsaw under grant #G33-7.

## REFERENCES

- [1] Evans, D., “A new type of magnetic balance,” J. Phys. E: Sci. Instrum. 7, 247 (1974).

- [2] Pendry, J., Holden, A., Robins, D., and Stewart, W., “Magnetism from conductors and enhanced nonlinear phenomena,” *IEEE Trans. on Microwave Theory and Tech.* 47, 2075–2084 (1999).
- [3] Wiltshire, M., Pendry, J., Young, I., Larkman, D., Gilderdale, D., and Hajnal, J., “Microstructured magnetic materials for RF flux guides in magnetic resonance imaging,” *Science* 291, 849–851 (2001).
- [4] Smith, D., Padilla, W., Vier, D., Nemat-Nasser, S., and Schultz, S., “Composite medium with simultaneously negative permeability and permittivity,” *Phys. Rev. Lett.* 84, 4184–4187 (2000).
- [5] Yen, T., Padilla, W., Fang, N., Vier, D., Smith, D., Pendry, J., Basov, D., and Zhang, X., “Terahertz magnetic response from artificial materials,” *Science* 303, 1494–1496 (2004).
- [6] Linden, S., Enkrich, C., Wegener, M., Zhou, J., Koschny, T., and Soukoulis, C. M., “Magnetic response of metamaterials at 100 THz,” *Science* 306, 1351–1353 (2004).
- [7] Zhang, S., Fan, W., Panoiu, N., Malloy, K., Osgood, R., and Brueck, S., “Experimental demonstration of near-infrared negative-index metamaterials,” *Phys. Rev. Lett.* 95, 137404 (2005).
- [8] Kafesaki, M., Tsiapa, I., Koschny, N. K. T., Soukoulis, C., and Economou, E., “Left-handed metamaterials: The fishnet structure and its variations,” *Phys. Rev. B* 75, 235114 (2007).
- [9] Zhou, J., Koschny, T., Kafesaki, M., Economou, E., Pendry, J., and Soukoulis, C., “Saturation of the magnetic response of split-ring resonators at optical frequencies,” *Phys. Rev. Lett.* 95, 223902 (2005).
- [10] Ishikawa, A., Tanaka, T., and Kawata, S., “Negative magnetic permeability in the visible light region,” *Phys. Rev. Lett.* 95, 237401 (2005).
- [11] Peng, L., Ran, L., Chen, H., Zhang, H., Kong, J., and Grzegorzczak, T., “Experimental observation of left-handed behavior in an array of standard dielectric resonators,” *Phys. Rev. Lett.* 98, 157403 (2007).
- [12] Schuller, J., Zia, R., Tauber, T., and Brongersma, M., “Dielectric metamaterials based on electric and magnetic resonances of silicon carbide particles,” *Phys. Rev. Lett.* 99, 107401 (2007).
- [13] Zhao, Q., Kang, L., Du, B., Zhao, H., Xie, Q., Huang, X., Li, B., Zhou, J., and Li, L., “Experimental demonstration of isotropic negative permeability in a three-dimensional dielectric composite,” *Phys. Rev. Lett.* 101, 027402 (2008).
- [14] Popa, B. and Cummer, S., “Compact dielectric particles as a building block for low-loss magnetic metamaterials,” *Phys. Rev. Lett.* 100, 207401 (2008).
- [15] Vynck, K., Felbacq, D., Centeno, E., Cabuz, A., Cassagne, D., and Guizal, B., “All-dielectric rod-type metamaterials at optical frequencies,” *Phys. Rev. Lett.* 102, 133901 (2009).
- [16] Xiao, S., Chettiar, U., Kildishev, A., Drachev, V., Khoo, I., and Shalae, V., “Tunable response of metamaterials,” *Appl. Phys. Lett.* 95, 033115 (2009).
- [17] Mirin, N., Ali, T., Nordlander, P., and Halas, N., “Perforated semishells: far-field directional control and optical frequency magnetic response,” *ACS Nano* 4, 2701–2712 (2010).
- [18] Jeyaram, Y., Jha, S., Agio, M., Löffler, J., and Ekinici, Y., “Magnetic metamaterials in the blue range using aluminum nanostructures,” *Opt. Lett.* 35, 1656–1658 (2010).
- [19] Buresi, M., van Oosten, D., Kampfrath, T., Schoenmaker, H., Heideman, R., Leinse, A., and Kuipers, L., “Probing the magnetic field of light at optical frequencies,” *Science* 326, 550–553 (2009).
- [20] Buresi, M., Kampfrath, T., van Oosten, D., Prangma, J., Song, B., Noda, S., and Kuipers, L., “Magnetic light-matter interactions in a photonic crystal nanocavity,” *Phys. Rev. Lett.* 105, 123901 (2010).
- [21] Vignolini, S., Intonti, F., Riboli, F., Balet, L., Li, L., Francardi, M., Gerardino, A., Fiore, A., Wiersma, D., and Gurioli, M., “Magnetic imaging in photonic crystal microcavities,” *Phys. Rev. Lett.* 105, 123902 (2010).
- [22] Zhan, Q., “Cylindrical vector beams: from mathematical concepts to applications,” *Adv. Opt. Photon.* 1, 1–57 (2009).
- [23] Banzer, P., Peschel, U., Quabis, S., and Leuchs, G., “On the experimental investigation of the electric and magnetic response of a single nano-structure,” *Opt. Express* 18, 10905–10923 (2010).
- [24] Antosiewicz, T. J., Wróbel, P., and Szoplik, T., “Magnetic field concentrator for probing optical magnetic metamaterials,” *Opt. Express* 18, 25906–25911 (2010).
- [25] Antosiewicz, T. and Szoplik, T., “Corrugated metal-coated tapered tip for scanning near-field optical microscope,” *Opt. Express* 15, 10920–10928 (2007).
- [26] Antosiewicz, T. and Szoplik, T., “Corrugated SNOM probe with enhanced energy throughput,” *Opto-Electron. Rev.* 16, 451–457 (2008).

- [27] Antosiewicz, T., Wróbel, P., and Szoplik, T., “Performance of scanning near-field optical microscope probes with single groove and various metal coatings,” *Plasmonics* 6, 11–18 (2011).
- [28] Johnson, P. and Christy, R., “Optical constants of the noble metals,” *Phys. Rev. B* 6, 4370–4379 (1972).
- [29] Taflove, A. and Hagness, S., [Computational electrodynamics], Artech House, Norwood, MA, third ed. (2005).
- [30] Nerkararyan, K., “Superfocusing of a surface polariton in a wedge-like structure,” *Phys. Lett. A* 237, 103–105 (1997).
- [31] Stockman, M., “Nanofocusing of optical energy in tapered plasmonic waveguides,” *Phys. Rev. Lett.* 93, 137404 (2004).
- [32] Verhagen, E., Spasenovic, M., Polman, A., and Kuipers, L., “Nanowire plasmon excitation by adiabatic mode transformation,” *Phys. Rev. Lett.* 102, 203904 (2009).
- [33] Gramotnev, D. and Bozhevolnyi, S., “Plasmonics beyond the diffraction limit,” *Nature Photonics* 4, 83–91 (2010).
- [34] Bozhevolnyi, S. and Nerkararyan, K., “Adiabatic nanofocusing of channel plasmon polaritons,” *Opt. Lett.* 35, 541–543 (2010).